


ORIGINAL ARTICLE

Open Access



Mechanical characteristics of auxetic composite honeycomb sandwich structure under bending

Hang Hang Xu¹, Xue Gang Zhang¹, Dong Han¹, Wei Jiang¹, Yi Zhang¹, Yu Ming Luo¹, Xi Hai Ni¹, Xing Chi Teng¹, Yi Min Xie² and Xin Ren^{1*} 

Abstract

Auxetic honeycomb sandwich structures (AHS) composed of a single material generally exhibit comparatively lower energy absorption (EA) and platform stress, as compared to traditional non-auxetic sandwich structures (TNS). To address this limitation, the present study examines the use of aluminum foam (AF) as a filling material in the re-entrant honeycomb sandwich structure (RS). Filling the AHS with AF greatly enhances both the EA and platform stress in comparison to filling the TNS with AF, while the auxetic composite honeycomb sandwich structure effectively addresses interface delamination observed in traditional non-auxetic composite sandwich structures. Subsequently, the positive–negative Poisson's ratio coupling designs are proposed to strengthen the mechanical features of a single honeycomb sandwich structure. The analysis results show that the coupling structure optimizes the mechanical properties by leveraging the high bearing capacity of the hexagonal honeycomb and the great interaction between the re-entrant honeycomb and the filling material. In contrast with traditional non-auxetic sandwich structures, the proposed auxetic composite honeycomb sandwich structures demonstrate superior EA and platform stress performance, suggesting their immense potential for utilization in protective engineering.

Keywords Auxetic, Energy absorption, Mechanical metamaterial, Aluminum foam, Re-entrant, Three-point bending

1 Introduction

The sandwich structure, comprised of a lightweight core material sandwiched between rigid stiff face-sheets, is popularly used in protective engineering as it offers exceptional specific stiffness and energy absorption (EA) properties (Bohara et al., 2023; Ma et al., 2021; Wang et al., 2022; Xia et al., 2022a, 2022b; Zhang et al., 2023). The mechanical features of sandwich structures are impacted by the geometrical properties of core and

face-sheets. There are many types of cores, including Y shape, metal foam, honeycomb, and corrugation (Boonkong et al., 2016; Rubino et al., 2010; Vidwans et al., 2023; Yan et al., 2022), etc. Among these, honeycomb sandwich structures have attracted the most attention, due to their superior EA, improved stiffness and enhanced strength. He et al. (2019) carried out a succession of three-point flexural testing and low-speed impact testing to examine the effects of residual bending strength and impact-induced damage characteristics of honeycomb sandwich panels. Wang et al. found that the indentation of ceramic sandwich occurs in the area near the two supports subjected to bending loads (Wang et al., 2019a, 2019b). As discovered subsequently, the geometric configuration had a major impact in ascertaining the bending performance of ceramic honeycomb sandwich panels (Wang et al., 2019a, 2019b). The mechanical

*Correspondence:

Xin Ren
xin.ren@njtech.edu.cn

¹ Centre for Innovative Structures, College of Civil Engineering, Nanjing Tech University, Nanjing 211816, Jiangsu, People's Republic of China

² Centre for Innovative Structures and Materials, School of Engineering, RMIT University, Melbourne 3001, Australia



© The Author(s) 2024. **Open Access** This article is licensed under a Creative Commons Attribution 4.0 International License, which permits use, sharing, adaptation, distribution and reproduction in any medium or format, as long as you give appropriate credit to the original author(s) and the source, provide a link to the Creative Commons licence, and indicate if changes were made. The images or other third party material in this article are included in the article's Creative Commons licence, unless indicated otherwise in a credit line to the material. If material is not included in the article's Creative Commons licence and your intended use is not permitted by statutory regulation or exceeds the permitted use, you will need to obtain permission directly from the copyright holder. To view a copy of this licence, visit <http://creativecommons.org/licenses/by/4.0/>.

properties of sandwich panels made of short-aramid-fiber were investigated at diverse loading velocities (Sun et al., 2021). Moreover, a comparative analysis was carried out on the flexure and mechanical properties of sandwich structures incorporating multiple honeycomb cores as opposed to those featuring a single-core in conventional sandwich panels (Naresh et al., 2021). It is noteworthy that the investigated sandwich configurations predominantly consist of either singular homogeneous material or multiple layers of composite material. Despite this, the load-bearing capabilities of the core material remain constrained.

Compared to multi-layer composites, honeycomb sandwich structures filled with soft materials offer desirable mechanical properties. The reason is that the filler in the composite honeycomb sandwich plate is placed in the honeycomb core, which leads to the generation of additional interaction forces between the filler and the honeycomb. According to a comparative study of different kinds of corrugated sandwich panels (Hamidin et al., 2021), it was found that the incorporation of polyurethane foam significantly enhances the EA. Nevertheless, the non-auxetic honeycomb structure has a minor interaction effect with the internal filling material, potentially leading to interface delamination.

Negative Poisson's ratio materials, known as "auxetics" (Evans et al., 1991), are a type of mechanical metamaterials (Asad et al., 2020; Coulais et al., 2018; Pan et al., 2024) that exhibit the unusual trait of expanding when stretched and contracting when compressed. This distinctive behavior creates a strong interplay between auxetics and the internal filling materials, setting them apart from conventional engineering materials (Lv et al., 2020; Zhao et al., 2021). The superior properties of auxetics in terms of EA have led to extensive research and initial applications in protective engineering domains (Ni et al., 2023; Foster et al., 2018; Ren et al., 2018), such as honeycomb sandwich structures (Xia et al., 2022a, 2022b). In a comprehensive study on engineered graded cellular architectures, an in-depth analysis of the bending response and failure mechanisms was conducted (Hou et al., 2013). The research highlighted the significant impact of gradient extent and the aspect ratio of the auxetic unit cells with angle gradient cores on the mechanical features of the sandwich panels, based on their topology. Li et al. (2022) evaluated the effects of different factors on the failure mode, deformation behavior, and mechanical features of sandwich panels with non-auxetic and auxetic honeycomb cells. Geramizadeh et al. (2022) analyzed the impact of face-sheet thickness in sandwich beams, including re-entrant honeycomb and hexagonal honeycomb, on switching failure mechanisms and EA growth rate. Subsequently, the impact resilience

of auxetic honeycomb sandwich panels coated with polyurea was analyzed. It was found that the back-side coated sandwich panels achieve the most excellent impact resistance (He et al., 2023). A proposal for a research project centered on multilayer composites incorporating a specially designed auxetic core was put forward, with a detailed analysis of the influence of thin facings on mechanical properties (Peliński & Smardzewski, 2022). It is worth noting that most of these studies focus on out-of-plane bending and transverse bending, and the potential of auxetic sandwich structures for longitudinal bending is still at an early stage.

At the present stage, the development of auxetic structures is hindered by two major challenges: low stiffness and low bearing capacity. These limitations have impeded the widespread application of auxetic structures across various fields. To address these challenges, researchers have been actively exploring methods to overcome these challenges by enhancing overall stiffness without compromising the auxetic effect. One notable approach proposed by Luo et al. (2022) involves combining the auxetic structure with slow recovery foam to enhance the stability of deformation and the EA property. Mechanical properties of aluminum foam (AF) filled auxetic honeycomb subjected to axial compression was subsequently explored. The findings indicate that the AF and auxetic honeycomb exhibit a stronger interaction compared to the non-auxetic honeycomb. Additionally, the auxetic composite structure enhanced the EA, while still preserving its auxetic properties (Xu et al., 2023).

While there exist diverse kinds of auxetic cells (Gao et al., 2020, 2023), the re-entrant honeycomb (Chen & Wang, 2022) has garnered considerable interest owing to its pronounced auxetic effect and relatively uncomplicated manufacturing process. In this study, the aluminum foam-filled re-entrant honeycomb sandwich structure (FRS), which corresponds to a double-layer sandwich plate (Li et al., 2023) in structural form, was manufactured and studied to improve the mechanical features of the re-entrant honeycomb under longitudinal bending. The deformation pattern, EA property, and longitudinal bending resistance of FRS were studied by comparing it with an aluminum foam-filled hexagonal honeycomb sandwich structure (FHS). Moreover, the effect of dimension parameters on both the EA and bending performance was discussed in the parameter study. Finally, novel coupling structures were devised and studied in order to optimize the structural mechanical features.

2 Approach to design and fabrication

2.1 Design of basic cell

Two types of common honeycomb structures were selected for this study, namely the non-auxetic hexagonal

honeycomb and auxetic re-entrant honeycomb according to the configuration of basic cells (Fig. 1). In order to facilitate a fair comparison between the two cell types, an identical rectangular design layout was employed for both. The size parameters of basic cells are displayed

in Table 1 to provide a clear understanding of their characteristics.

In this work, a two-step process was utilized to integrate the face-sheets and core of the sandwich structure as depicted in Fig. 2. Initially, the two types of

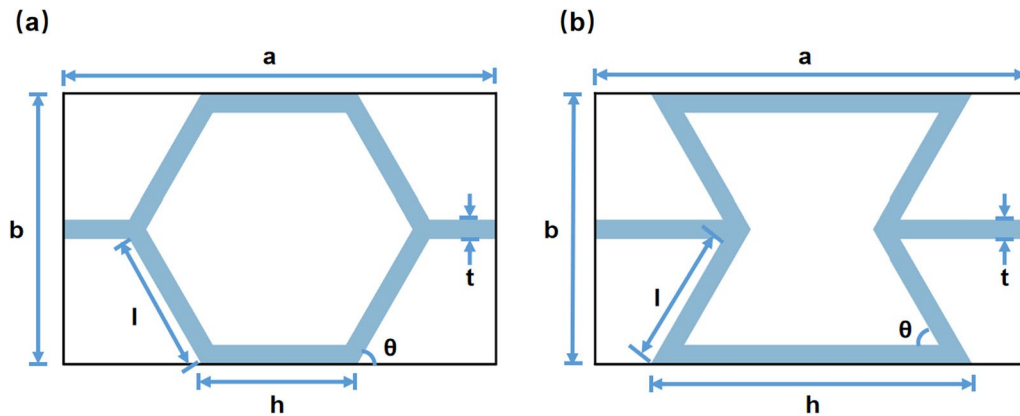


Fig. 1 Geometrical dimensions of the basic cell of **a** hexagonal honeycomb and **b** re-entrant honeycomb

Table 1 Geometrical parameters of the basic cells

Specimen	<i>a</i> (mm)	<i>b</i> (mm)	<i>h</i> (mm)	<i>l</i> (mm)	<i>t</i> (mm)	θ (°)	Porosity (%)	Relative density (%)
Re-entrant	22.27	13.86	16.58	7.42	1.00	60	0.83	0.17
Hexagonal	22.27	13.86	8.00	7.42	1.00	60	0.76	0.24

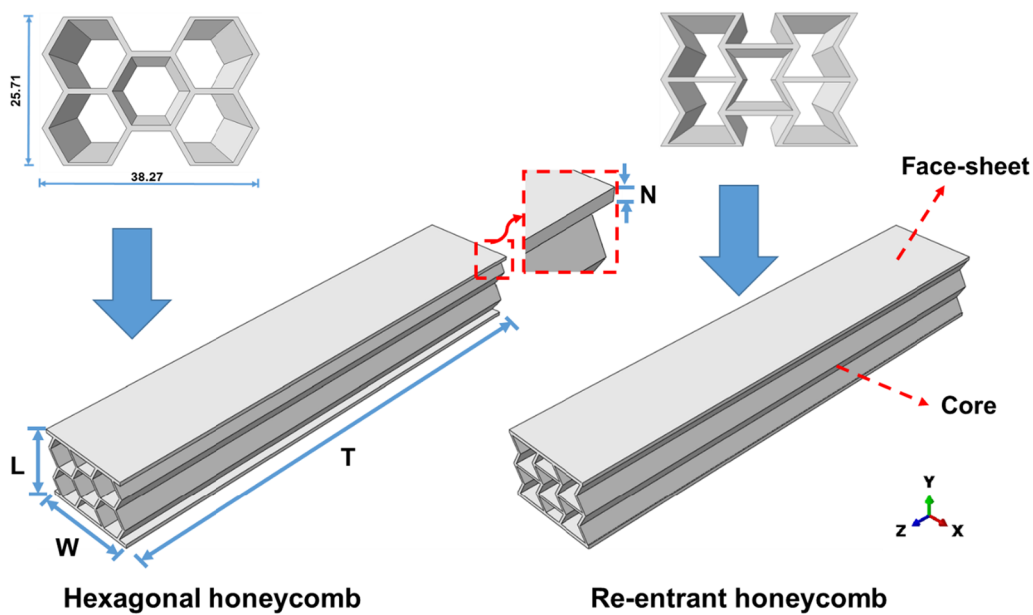


Fig. 2 The dimension of the honeycomb sections and sandwich structures

basic cells were arrayed to form honeycomb structures with 2×2 basic cells, all possessing identical cross-section dimensions. Subsequently, these honeycomb structures were employed as the core, with rectangular components acting as the face-sheets. This integration approach maintains the integrity and stability of the structure.

The face-sheet thickness N is 1.50 mm, and the structures with 2×2 basic cells were extended to a length of 200 mm in the Z direction. The length, width, and height of each structure are $T=200$ mm, $W=38.27$ mm, and $L=27.71$ mm, respectively. The structures were fabricated using solid 316L stainless steel pieces by wire cutting technology. Notably, the face-sheets and core were manufactured as one unit, eliminating the need for welding or adhesive bonding.

2.2 Fabrication of aluminum foam-filled honeycombs

Aluminum foam (AF) is characterized by its highly porous structure, which imparts several advantageous properties such as low density, superior EA performance, and high specific stiffness. These remarkable properties make AF an attractive material for applications requiring energy absorption. However, the rough surface of AF poses challenges for its direct use in civil engineering and protection fields. By incorporating AF as a filler in the voids of sandwich structures, it proves to be a strategic solution in overcoming these inherent limitations, and significantly elevates the overall performance of the structures, particularly in terms of EA, damping, and acoustic performance. Therefore, in this study, AF was selected as the filling material and shaped into two types of honeycombs through wire cutting. Subsequently, the honeycomb-shaped AF was manually inserted into the respective honeycomb frames without the use of any binders (Fig. 3).

3 Characteristics of the material

3.1 Tests of stainless steel specimens

Three specimens, each 1 mm thick, were manufactured in accordance with the ASTM E8M-2004 standard for conducting a tensile test on 316L stainless steel. The dimensional details of the specimens can be observed in Fig. 4. The specimens were produced using a wire-cutting technique that utilizes electrical spark discharge between the fine wire electrode and the workpiece to melt and cut the metal with precision. The tensile testing was executed on all specimens at a constant velocity of 2 mm/min. The primary objective of performing uniaxial tensile tests on the stainless steel specimens was to derive a constitutive model. This model would subsequently be employed in simulations and parametric analyses to predict the mechanical behavior. The density of the stainless steel specimen was measured at 7930 kg/m^3 . Stainless steel can be characterized by an elastic modulus of 190 GPa, a Poisson's ratio of 0.29, and a yield stress of 470.36 MPa (Fig. 5).

3.2 Tests of aluminum foam

Following the ASTM D1621-10 Standard, three cubic samples with dimensions of $50 \text{ mm} \times 50 \text{ mm} \times 50 \text{ mm}$ (Fig. 6) were fabricated. In order to achieve the material properties of AF, samples were underwent quasi-static uniaxial compression testing using an MTS testing machine. The samples were subjected to a constant loading rate of 3 mm/min (Fig. 6). The AF material exhibited a density of 660 kg/m^3 , an elastic modulus of 509.6 MPa (Fig. 7), and a plastic Poisson's ratio of 0.

4 Experimental setup and corresponding simulations

4.1 Experimental setup

The mechanical properties of four different types of sandwich structures were assessed by conducting three-point bending tests (Fig. 8), employing a universal testing machine (SUNS WDW-100). The test machine has

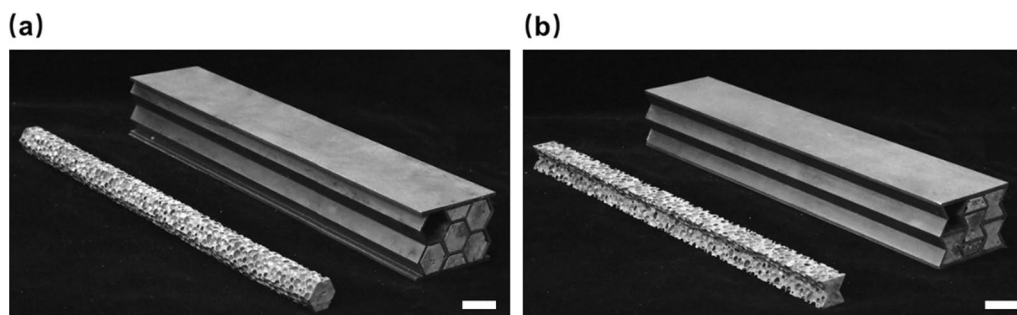


Fig. 3 **a** Manufacture of aluminum foam-filled hexagonal honeycomb sandwich structure (FHS) and **b** aluminum foam-filled re-entrant honeycomb sandwich structure (FRS) (scale bar: 20 mm)

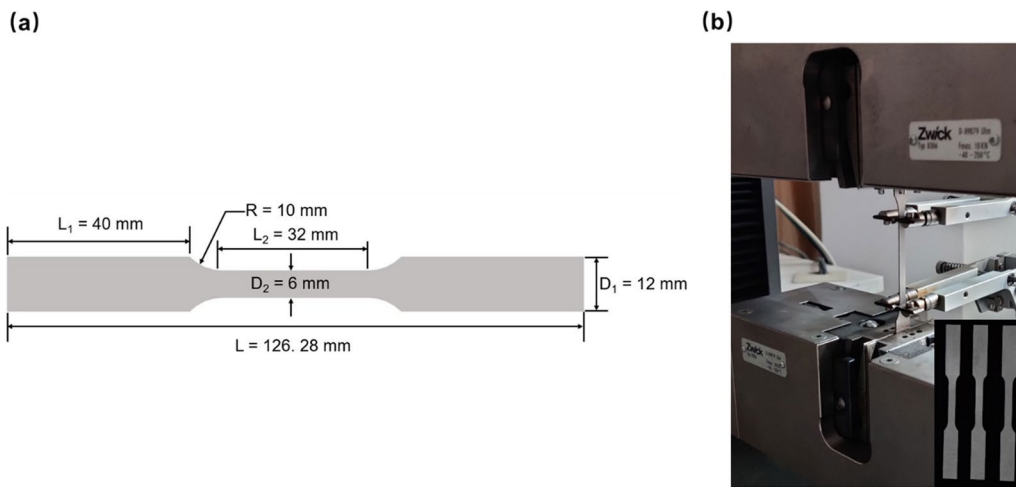


Fig. 4 a The specimen dimensions and b tensile strength testing of stainless steel samples

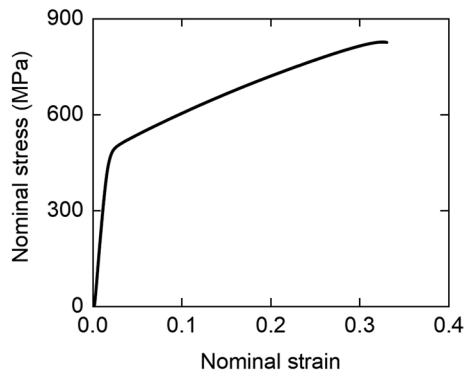


Fig. 5 Stress-strain relationship of 316L stainless steel

quasi-static loading conditions, thereby ensuring accurate measurement and analysis. Both the supports and indenter were of a 30 mm diameter \varnothing . The distance h of 150 mm between the two supports was maintained during the experiment. To capture the deformation behavior of the specimens during the mechanical testing, a camcorder was utilized to document the testing procedure. A schematic representation of the size parameters is provided in Fig. 8b.

Energy absorption (EA) of specimens is quantified as the total external energy that is dissipated during an impact event. This quantity is typically derived by integrating the load–deflection curve:

$$EA = \int_0^d f(x)dx, \tag{1}$$

a maximum load capacity of 100 kN and was operated at a consistent loading speed of 3 mm/min throughout the testing process. This loading speed was chosen to mimic

where d is the deflection of the indenter, and $f(x)$ is the correlation between load and deflection.

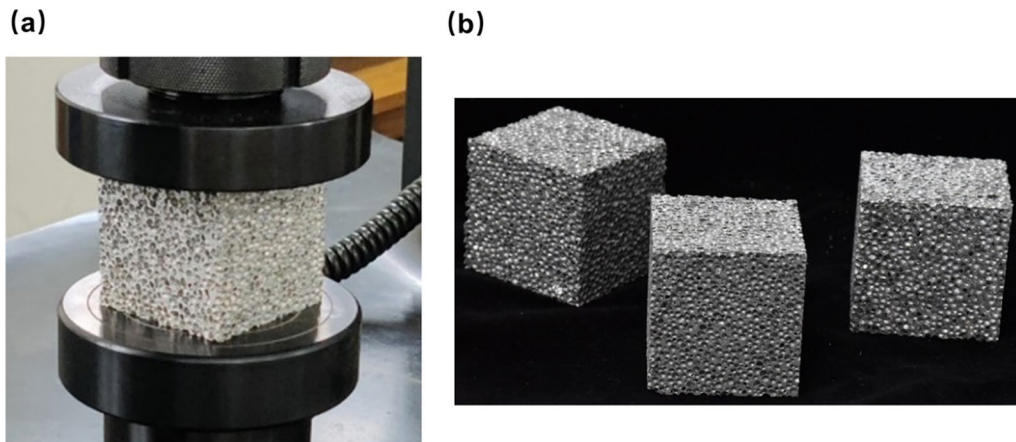


Fig. 6 a Compressive strength testing of aluminum foam (AF) and b three cubic samples of AF

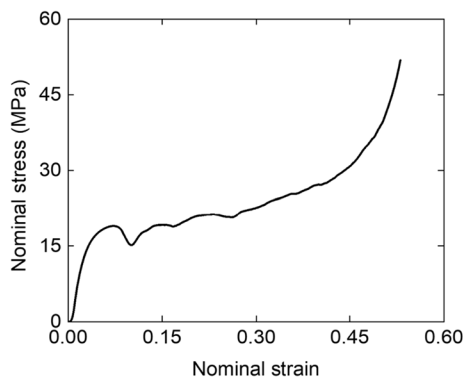


Fig. 7 Stress–strain relationship of AF

Specific energy absorption (SEA) is defined as the EA per unit mass. It is typically calculated by dividing the EA by the weight of the structural component.

$$SEA = \frac{EA}{m}. \tag{2}$$

Peak crushing force (PCF) refers to the maximum force during bending. As a protective structure, it is unfavorable when the value of PCF is too large. Mean crushing force (MCF) indicates the EA per unit displacement b of the indenter.

$$MCF = \frac{EA}{b}. \tag{3}$$

Crush force efficiency (CFE) is the ratio of the MCF to the PCF and is always used to measure the protection ability of a structure. The greater the CFE value, the higher the protective effect.

$$CFE = \frac{MCF}{PCF}. \tag{4}$$

4.2 Finite element simulations

To further assess the mechanical property of the structures, finite element models were generated with identical dimensions to those used in the experiments and numerical simulations. These models were analyzed using Abaqus/Explicit 6.14, a commercial finite element software solver. To capture the behavior of the stainless steel, an isotropic elastic–plastic model was employed, and the material parameters were obtained from the tensile test from Sect. 3.1. For the analysis of the AF, a crushable foam material model was utilized, and the material parameter was deduced from the compression test described in Sect. 3.2. To simulate the compression process, the structure was subjected to compression between two analytical rigid bodies: supports and an indenter. To facilitate the application of boundary conditions, three reference points were placed in both the supports and the indenter, which facilitates adding the arrangement of boundary conditions. The supports were fixed and the indenter underwent a displacement of 18 mm. General contact properties were employed for interactions between various components in the simulation. This encompasses contacts between the indenter and structures, supports and structures, as well as the structures and AF. A tangential friction coefficient of 0.3 was specifically assigned to accurately simulate the interactions between the components. Moreover, normal contact was modeled as hard contact to mitigate penetration of the structural elements.

A hexahedral mesh (C3D8R) is utilized for numerical modeling of both the honeycomb sandwich structures and the AF. To achieve an optimal mesh distribution, a symmetric gradient mesh approach was adopted after performing a convergence analysis of the RS and AF. This approach involved increasing the mesh density in regions characterized by high stress concentration (such as near

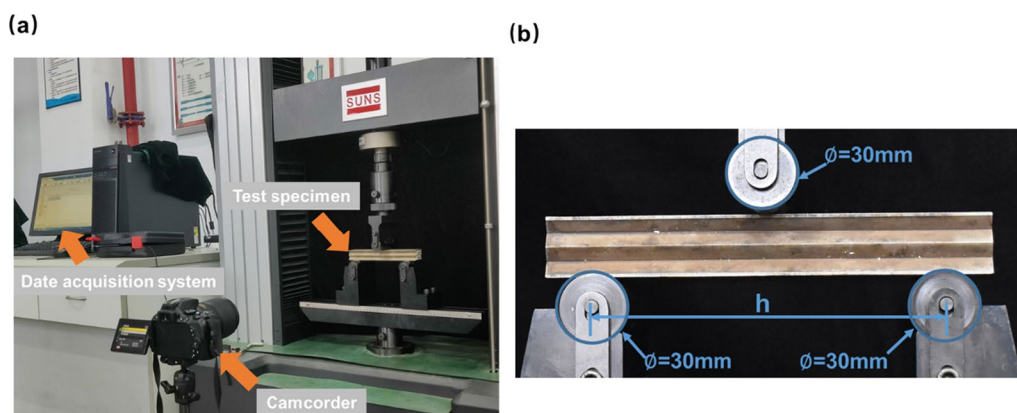


Fig. 8 **a** Experimental layout and **b** size parameter information

the indenter) and decreasing the mesh density in other parts (Fig. 9). The approximate global mesh size for the honeycomb sandwich structures was set as 0.35 mm. Additionally, the element size of the AF mesh was determined to be 1.5 mm. These specific configurations can balance computational efficiency and accuracy.

5 Results and discussion

Upon subjecting the specimens to an indenter displacement of 18 mm, the deformation patterns of four different sandwich structures were obtained, as illustrated in Fig. 10. Despite the manifestation of cracks in proximity to the center of the bottom face-sheet of the re-entrant honeycomb sandwich structure (RS) during the experiment, the observed overall experimental deformation pattern corresponded well with the numerical simulations. This manifestation can be attributed to defects in the wire-cutting process. Notably, in the process of bending, the AF was noticeably squeezed out of the honeycomb to a greater extent in FRS in comparison to the

hexagonal honeycomb sandwich structure (HS). This behavior is likely due to the more effective interaction between the AF and the RS in contrast to the HS.

To demonstrate the deformation patterns of the mid-span sections, finite element analysis was employed, yielding deformation patterns as depicted by the red dashed lines in Fig. 10. Due to the auxetic effect, the auxetic core of the RS shrinks inward, while the non-auxetic core in the HS squeezes and bends to both sides. Similarly, the auxetic core exhibits an inward contraction mechanism, thereby imposing constraints on the adjacent AF inside the FRS due to the auxetic effect. However, conspicuous interface delamination is observed in the FHS, indicating incomplete interfacial contact between the non-auxetic core and the AF.

The parameter denoted as the bending angle θ (Fig. 11) represents the angular deviation between the bottom face-sheet and the horizontal plane of the structure. A larger bending angle denotes a more pronounced curvature at the two ends of the structure.

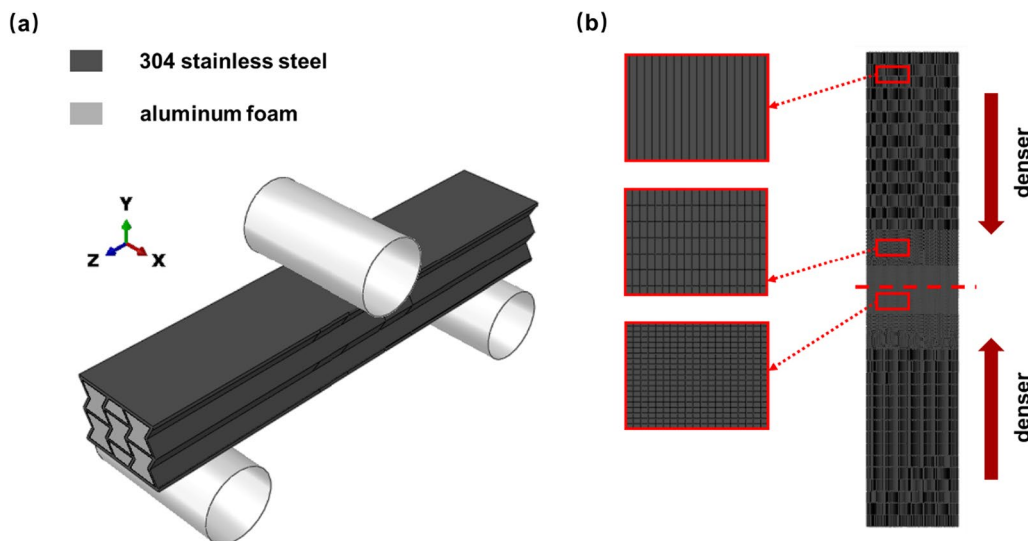


Fig. 9 **a** Finite element model and **b** gradient mesh (detail in red lines) of the RS

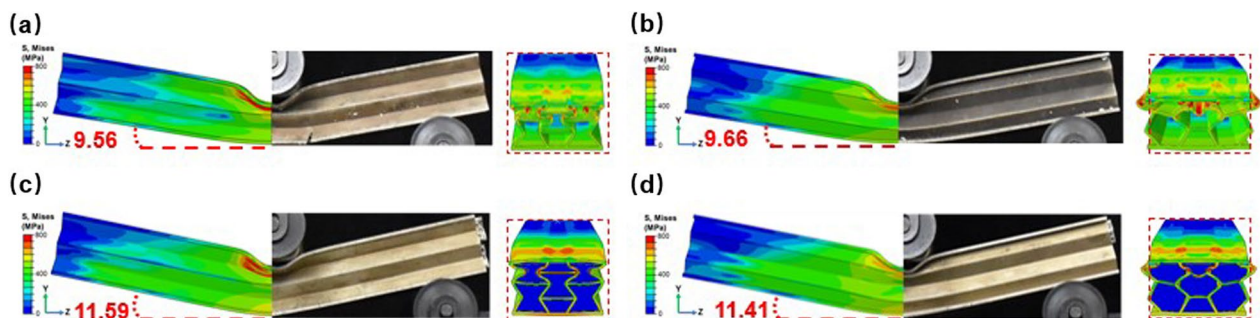


Fig. 10 Deformation patterns and mid-span sections (in red dashed lines) for **a** RS, **b** HS, **c** FRS, and **d** FHS

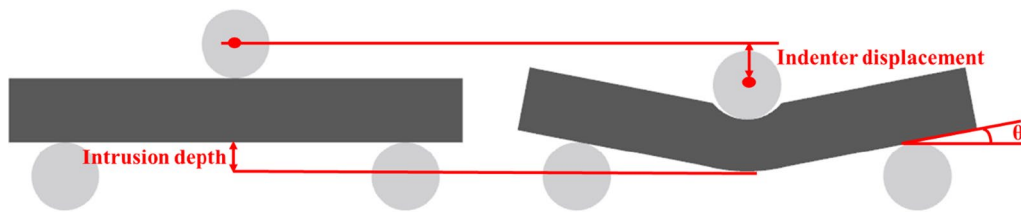


Fig. 11 Illustration of the bending angle θ and the intrusion depth

For the RS and HS specimens, the bending angles are measured at 9.56° and 9.66° , respectively, which indicates that HS produces a more pronounced bending. Following the infusion with AE, the bending angles for the FRS and FHS configurations are determined as 11.59° and 11.41° , respectively, representing an increase in bending angles post-treatment. The intrusion depth is another index to reflect the flexural performance of the structures, wherein a greater intrusion depth stands for heightened bending, primarily localized at the midpoint of the structures (Xia et al., 2022a, 2022b). In this study, the term “intrusion depth” (Fig. 11) refers to the displacement observed at the midpoint of the bottom face-sheet when the indenter displacement attains 18 mm. The simulation results reveal intrusion depths of 9.45 mm, 9.39 mm, 12.49 mm and 11.85 mm for RS, HS, FRS, and FHS, respectively. It can be observed that the intrusion depth undergoes a substantial increase after filling the AE.

The comparison of the load–deflection curves for four distinct structures subjected to three-point bending and computational simulation is depicted in Fig. 12. In this study, deflection specifically denotes the indenter deflection. The bending response observed in the experimental data aligns well with the finite element curve across the four different honeycomb sandwich structures, including elastic modulus and platform stress, indicating a consistent correlation between experimental data and finite element analysis results. However, owing to the transverse bending (Fig. 15) of the bottom face-sheet, the simulation curve exhibits a slightly greater magnitude than the experimental curve at the later stage of deformation subsequent to being filled with AE.

An obvious difference in the boundary conditions (Fig. 13) between the experiment and the simulation is noted in the vicinity of the indenter. In the simulation setting, the indenter is completely immersed in the upper face-sheet, whereas in the experimental setup, the

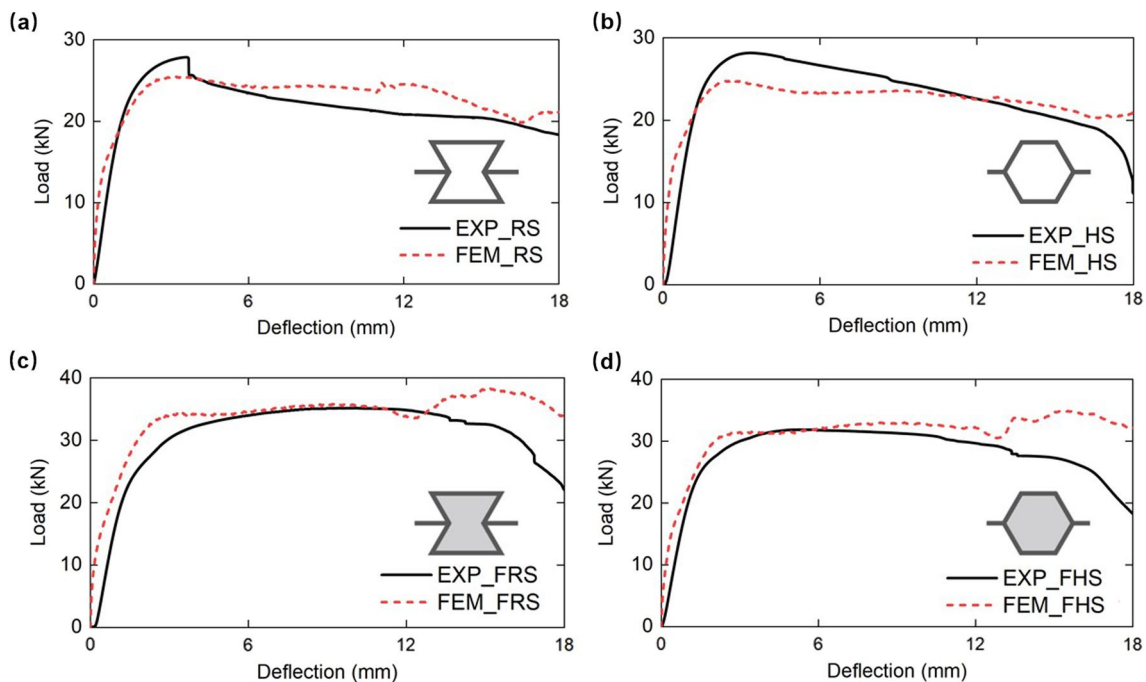


Fig. 12 Comparison of the load–deflection curves for **a** RS, **b** HS, **c** FRS and **d** FHS between simulations and experiments

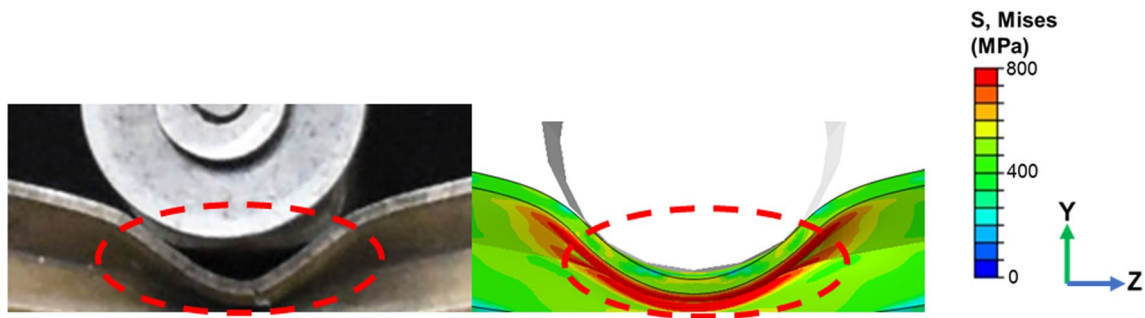


Fig. 13 Difference in boundary conditions between the experiment and the simulation

indenter does not establish complete contact with the upper face-sheet. This variance may be ascribed to the inherent imperfections present in the experimental materials relative to the ideal conditions assumed in the simulation. As a result, the bending angles derived from the experimental data are slightly larger than those predicted by the simulation.

The platform stage of the structures achieves stabilization post-filling, but the bearing capacity of FRS manifests a more substantial increment compared to that of FHS. This observed phenomenon underscores the superior performance of the interaction between the auxetic honeycomb and the AF. This can be interpreted as the auxetic honeycomb restraining the deformation of AF, while the AF provides support for the auxetic honeycomb.

Unlike quasi-static compression, the SEA of RS is lower than that of HS (Table 2), because only part of the structure is deformed during bending. However, the SEA of RS surpasses that of HS upon the incorporation of AF into both kinds of honeycomb sandwich structures. Although SEA of FRS is slightly larger than that of FHS, their respective improvements post AF filling exhibit distinguishable characteristics.

The enhanced factor of EA of the structure post AF filling is defined as α through the formula:

$$\alpha = \frac{EA_2 - EA_1}{EA_1}, \tag{5}$$

where EA_1 and EA_2 are the values of energy absorption for the hollow and composite sandwich structures, respectively.

Likewise, the enhanced factor is extended to SEA, characterized as β according to the formula:

$$\beta = \frac{SEA_2 - SEA_1}{SEA_1}, \tag{6}$$

Table 2 Correlation between simulated and experimental mechanical properties in RS, HS, FRS and FHS

Design	Intrusion depth (mm)	Bending angle (°)	EA (J)	SEA (J/g)
EXP-RS	–	10.24	387.997	0.866
FEM-RS	9.45	9.56	413.425	0.92
EXP-HS	–	10.03	409.110	1.010
FEM-HS	9.39	9.66	401.648	0.99
EXP-FRS	–	11.81	552.150	1.026
FEM-FRS	12.49	11.59	608.881	1.132
EXP-FHS	–	12.01	500.960	1.004
FEM-FHS	11.85	11.41	562.720	1.128

where SEA_1 and SEA_2 are the values of specific energy absorption for the hollow and composite sandwich structures, respectively.

α (EA) and β (SEA) of FRS stand at 0.47 and 0.23 respectively, while those of FHS are measured at 0.40 and 0.14. Both enhanced factors of FRS are larger than those of FHS. Moreover, FRS exhibits a propensity for a larger cell count which subsequently results in an increased bending area, particularly enhancing its applicability in engineering scenarios. These findings underscore the superior performance of the re-entrant composite structure in bending situations compared with conventional composite honeycomb structures.

6 Finite element analyses

6.1 Finite element model validation

The numerical load–deflection curves obtained from the simulation bear a high level of consistency with the experimental outcomes as presented in Sect. 5. Compared with FHS, FRS has advantages in terms of EA and deformation pattern. Therefore, a parametric analysis of FRS is conducted in this section. The subsequent sections delve into the impact of the face-sheet thickness and the cell wall thickness. To qualitatively analyze the EA capacity of structures, five distinct energy absorption indices

are proposed, i.e., EA, mean crushing force (MCF), peak crushing force (PCF), crush force efficiency (CFE), and SEA. The bending performance is predominantly assessed based on the intrusion depth and bending angle.

6.2 Parametric studies of cell wall thickness

The sandwich structures' primary function is to absorb energy during the bending process, with the core playing a critical role as the main energy absorber. Consequently, the mechanical features of these structures are significantly affected by the geometrical parameters of the basic cell of the honeycomb core. In order to investigate the influence of the geometrical parameters of cells on the mechanical properties, four different cell wall thicknesses (1.0 mm, 1.4 mm, 1.8 mm, and 2.2 mm) were individually set, while keeping other parameters constant.

Figure 14 presents the patterns of structural deformation and mid-span sections for various cell wall thicknesses. As the cell wall thickness increases, both intrusion depth and bending angle (Table 3) of the structures significantly increase, indicating a more pronounced bending of the structure. The mid-span sections further reveal that a thicker cell wall diminishes the structural compressibility, thereby indicating a weakening of the auxetic effect.

The load–deflection curves of the four kinds of structures are displayed as Fig. 15. As the thickness of the cell wall is augmented, there is a commensurate enhancement in the stiffness of the structure. An evident peak force manifests initially when the thickness of the cell wall reaches 1.8 mm. Nevertheless, it is imperative to note that a substantial rise in the initial peak force is deemed unfavorable in the field of engineering protection.

An increase in cell wall thicknesses causes the progression of transverse bending in the bottom face-sheet. From the load–deflection curves, it is observable that the displacement during the second strengthening stage (deflection after the star) advances.

Elevated cell wall thicknesses result in higher EA and SEA values for the structures (Table 3). However, the increment in SEA gradually diminishes. This phenomenon may be elucidated by postulating that heightened cell wall thicknesses would lead to reduced filler content, as well as a decrease in the available shrinkage space of the AF. In addition, a notable surge in the value of PCF accompanies increments in cell wall thickness, thereby compromising the delicate balance between injury tolerance and EA capacity in protective engineering.

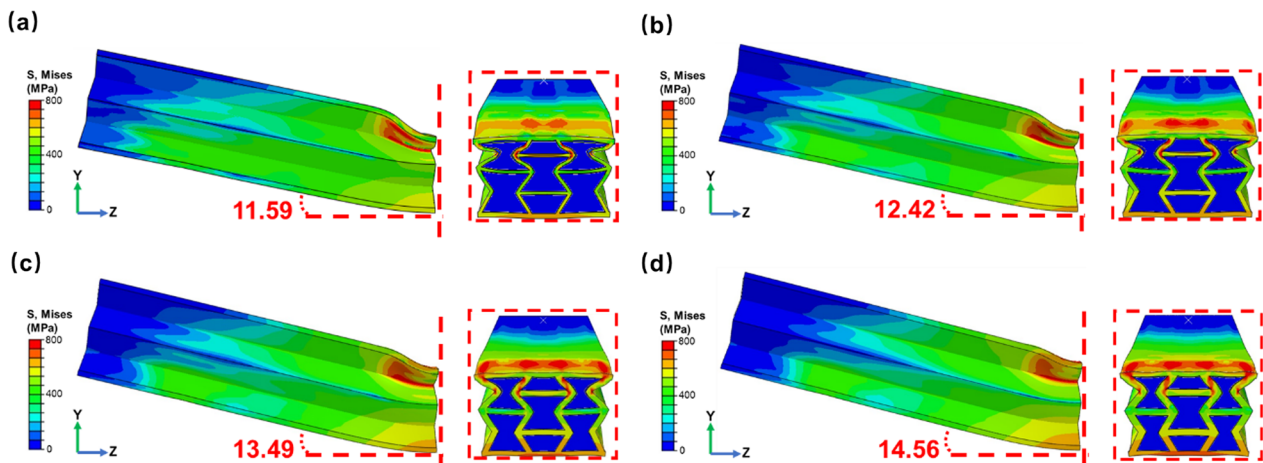


Fig. 14 Deformation patterns and mid-span sections in simulation for **a** 1.0 mm, **b** 1.4 mm, **c** 1.8 mm and **d** 2.2 mm

Table 3 Mechanical features of FRSs with varying cell wall thicknesses

Design	Intrusion depth (mm)	Bending angle (°)	EA (J)	MCF (kN)	PCF (kN)	CFE (%)	SEA (J/g)
1.0 mm	12.49	11.59	608.88	33.83	38.34	0.88	1.132
1.4 mm	13.57	12.42	766.05	42.56	49.99	0.85	1.214
1.8 mm	14.60	13.49	919.67	51.09	60.42	0.85	1.276
2.2 mm	15.40	14.56	1064.59	59.14	69.85	0.85	1.316

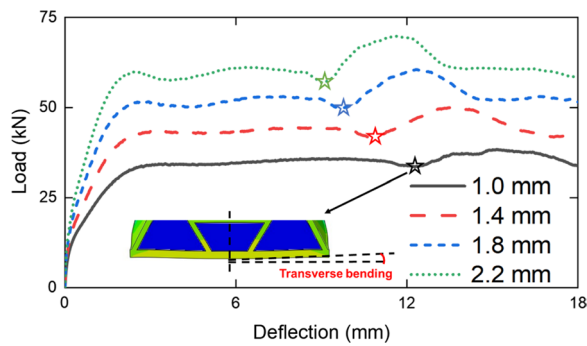


Fig. 15 Load–deflection curves of FRSs with various cell wall thicknesses (the stars in the figure indicate the beginning of transverse bending in the bottom face-sheet)

6.3 Parametric studies of face-sheet thickness

Considering that the face-sheet of the sandwich structure is the most severely bent part, this component serves as a critical determinant of the overall mechanical properties of the structure. To explore the correlation between face-sheet thickness and mechanical features, distinct face-sheet thicknesses of 1.2 mm, 1.5 mm, 1.8 mm, and 2.1 mm were examined, while

maintaining consistent dimensions for other structural components.

The deformation patterns and mid-span sections with various face-sheet thicknesses are illustrated in Fig. 16. Both intrusion depth and bending angle (Table 4) of the structures exhibit a pronounced decrease as face-sheet thickness increases. This phenomenon signifies an enhancement in the structure’s resistance to bending. Notably, analysis of the mid-span sections reveals that changes in face-sheet thickness yield minimal impact on the auxetic effect (Fig. 16).

From the load–deflection curves of the four sandwich structures displayed in Fig. 17, it is evident that the stiffness E and the platform stress of the structure exhibit an uptrend as the thickness of the face sheets increases, albeit the increase is relatively small. Observations of the load–deflection curves indicate a postponed onset of the secondary strengthening phase, implying that an increase in face-sheet thickness leads to a retardation in transverse bending in the bottom face-sheet.

After analysis, it is found that the trend of SEA exhibits an initial rise followed by a subsequent decline. This phenomenon underscores that a judicious augmentation in face-sheet thickness yields an amplification in SEA.

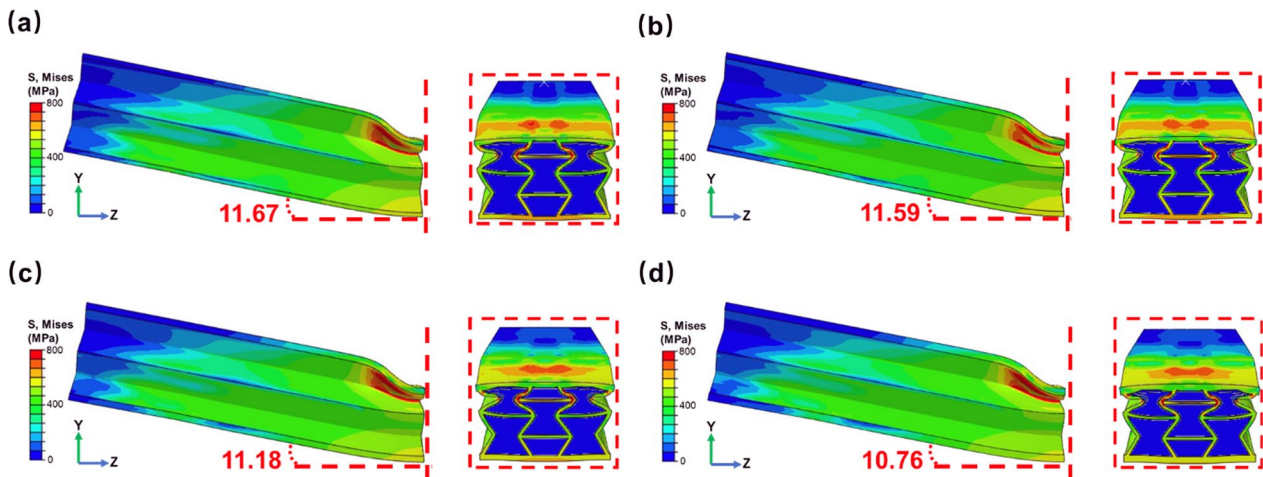


Fig. 16 Deformation patterns and mid-span sections in simulation for **a** 1.2 mm, **b** 1.5 mm, **c** 1.8 mm and **d** 2.1 mm

Table 4 Mechanical features of FRSs with varying face-sheet thicknesses

Design	Intrusion depth (mm)	Bending angle (°)	EA (J)	MCF (kN)	PCF (kN)	CFE (%)	SEA (J/g)
1.2 mm	12.56	11.67	598.95	33.28	38.37	0.87	1.126
1.5 mm	12.49	11.59	608.88	33.83	38.34	0.88	1.132
1.8 mm	12.16	11.18	638.06	35.45	38.85	0.91	1.123
2.1 mm	11.99	10.76	669.87	37.22	39.97	0.93	1.120

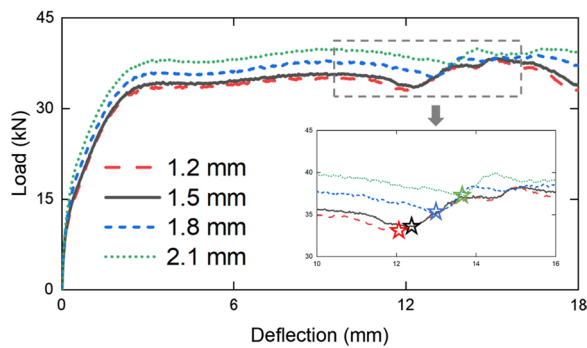


Fig. 17 Load–deflection curves of FRSs with various face-sheet thicknesses

However, the essential role of the face-sheet is to resist bending rather than absorb energy. Correspondingly, the increase of face-sheet thickness will inevitably reduce both the proportion of the internal honeycomb structure and the amount of filler material. Thus, it is evident that an excessive increase in the thickness of face-sheet will compromise the SEA performance of the overall structure.

6.4 Positive–negative Poisson’s ratio coupling structures

As analyzed in Sect. 5, the SEA of HS is higher than that of RS. However, following the introduction of fillings, the SEA of FRS exceeds that of FHS. This discrepancy can be attributed to the phenomenon of interface delamination occurring between the AF and the non-auxetic honeycomb inside the FHS. Such delamination indicates that the interaction force between the AF and the non-auxetic honeycomb is much smaller in comparison to those observed in the auxetic honeycomb. In order to mitigate the issue of interface delamination in FHS and enhance the EA performance, this section attempts to combine the auxetic honeycomb with the

non-auxetic honeycomb to design a positive–negative Poisson’s ratio coupling structure. Specifically, novel coupling architectures featuring a confluence of 1×2 non-auxetic honeycomb and 1×2 auxetic honeycomb are designed and investigated, as illustrated in Fig. 18. The cell dimensions of both honeycomb types adhere to the previously specified parameters, encompassing the three-dimensional dimensions of the structure, and the relative positions of the two kinds of honeycomb are also compared and analyzed.

Both the intrusion depth and bending angle of the newly designed positive–negative Poisson’s ratio coupling structures exhibit modest increments compared to those of the FRS (Fig. 19). However, the mid-span sections of the two coupling structures align closely with the delineation represented by the red dashed lines, indicating a tangible decrease in interfacial delamination. It is worth noting that segments of AF protrude from both coupling structures owing to the reinforcement effect, with this occurrence being more pronounced in the context of FPNS.

The stiffness and platform force of FPNS are significantly enhanced when compared with those of the FRS, while the load–deflection curves of the FRS and the FNPS exhibit similarities (Fig. 20). The findings confirm that the relative positions of non-auxetic honeycomb and auxetic honeycomb affect the mechanical features of the coupling structure. The bearing capacity of the non-auxetic frame is greater than that of the auxetic frame, thus enabling FPNS to withstand higher pressure levels during bending. Subsequent to the filling of foam, interface delamination manifests in the non-auxetic honeycomb, leading to a decrease in platform force. This occurrence can be mitigated through the reasonable combination of the two honeycomb types, thereby elucidating the benefits of FPNS. Moreover, both EA and SEA of FPNS are enhanced through the employment of this coupling methodology (Table 5).

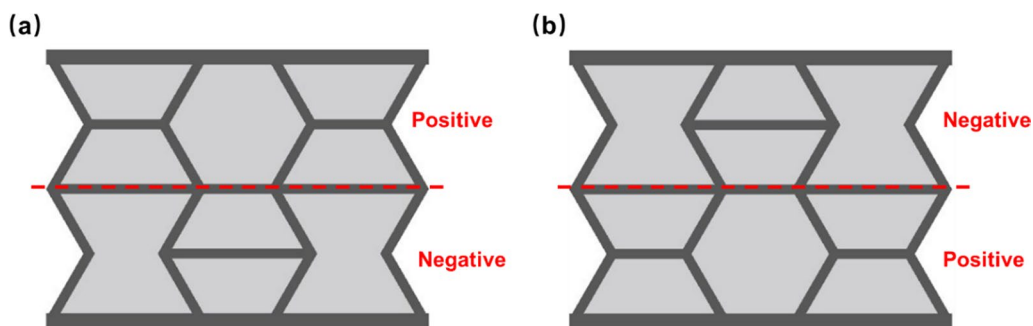


Fig. 18 The comparison of structural diagram for **a** aluminum foam-filled positive–negative Poisson’s ratio coupling sandwich structure (FPNS) and **b** aluminum foam-filled negative–positive Poisson’s ratio coupling sandwich structure (FNPS)

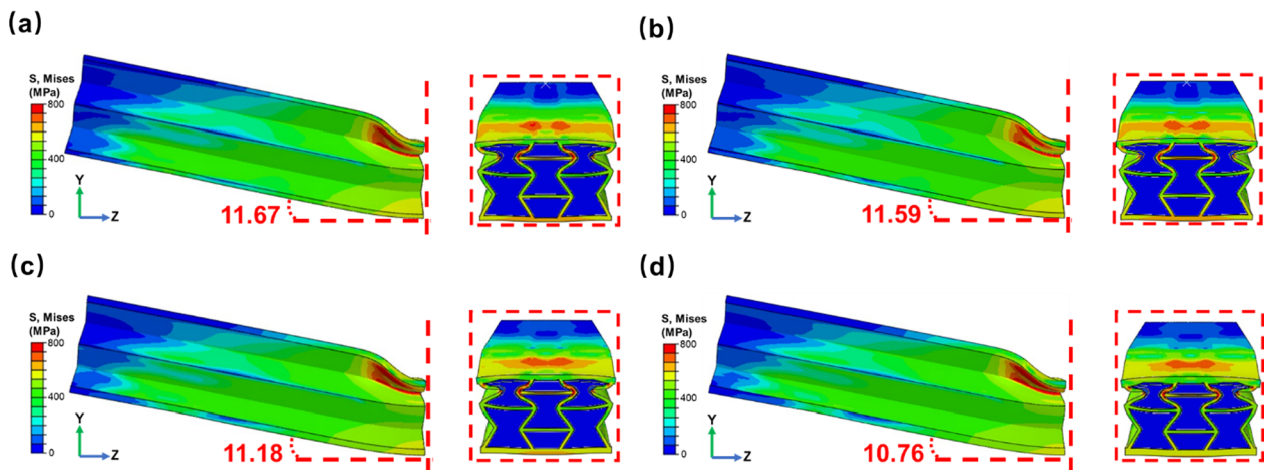


Fig. 19 Deformation patterns and mid-span sections in simulation for **a** FRS, **b** FHS, **c** FPNS and **d** FNPS

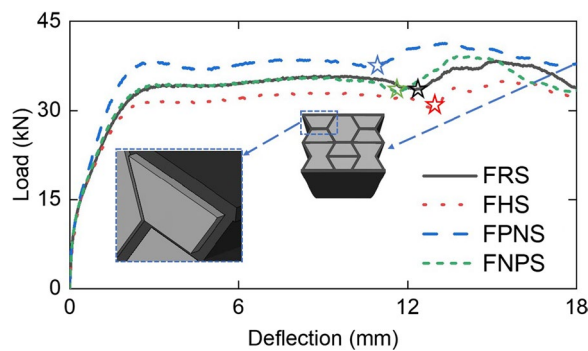


Fig. 20 Comparison of load–deflection curves of FRS, FHS, FPNS (AF is extruded out in blue dashed lines) and FNPS

7 Conclusions

In this study, we introduce a novel composite architecture comprising a re-entrant honeycomb sandwich structure (RS) integrated with aluminum foam (AF). Through a combination of simulations and experimental analyses, we investigate the bending properties, deformation pattern and energy absorption (EA) properties of this composite structure. The findings indicate that the aluminum foam-filled re-entrant honeycomb sandwich structure (FRS) exhibits notable advantages

in terms of superior EA performance and enhanced deformation behavior.

Furthermore, we conduct a comprehensive parametric analysis to elucidate the interplay between cell wall thickness, face-sheet thickness, and FRS. By assessing two key metrics, namely bending resistance and specific energy absorption (SEA), guidelines for optimal design are established. Within a specific range, increasing cell wall thickness leads to a reduction in bending resistance but a corresponding enhancement in SEA. Conversely, raising face-sheet thickness improves bending resistance but reduces SEA. Leveraging insights from the parametric study, we propose an optimized design configuration featuring a face-sheet thickness of 1.5 mm and a cell wall thickness of 1.0 mm. Lastly, our integrated design approach underscores the benefits of auxetic materials, which not only mitigate interface delamination but also enhance EA performance under a three-point bending load.

The proposed structure exhibits superior EA and deformation characteristics compared to monolithic materials and non-auxetic composite sandwich configurations. These desirable findings herald the potential of auxetic materials in advancing protective engineering applications.

Table 5 Mechanical features of FRS, FHS, FPNS and FNPS

Design	Intrusion depth (mm)	Bending angle (°)	EA (J)	MCF (kN)	PCF (kN)	CFE (%)	SEA (J/g)
FRS	12.49	11.59	608.88	33.83	38.34	88	1.132
FHS	11.85	11.41	562.72	31.26	34.96	89	1.128
FPNS	13.64	11.84	666.07	37.00	41.40	89	1.218
FNPS	12.95	11.72	608.20	33.79	39.16	86	1.112

Acknowledgements

This work was supported by the National Natural Science Foundation of China (Grant Number 51978330); Qing Lan Project of Jiangsu Province; Natural Science Foundation of Jiangsu Province (Grant Number BK20220103).

Author contributions

All authors participated in the study and supported the publication. Hang Xu: conceptualization, methodology, software, writing original draft. Xue Gang Zhang: investigation, validation, editing. Dong Han: investigation, validation, editing. Wei Jiang: investigation, validation. Yi Zhang: investigation, validation, editing. Yu Ming Luo: investigation, validation, editing. Xi Hai Ni: investigation, validation, editing. Xing Chi Teng: investigation, validation, editing. Yi Min Xie: validation, editing. Xin Ren: conceptualization, methodology, project administration, supervision, funding acquisition, editing, revision. All authors read and approved the final manuscript.

Data availability

All data generated or analyzed during this study are included in this article. Further inquiries can be directed to the corresponding author.

Declarations

Consent for publication

The manuscript is approved by all authors for publication.

Competing interests

The authors declare no competing interests.

Received: 12 December 2023 Revised: 30 March 2024 Accepted: 4 April 2024

Published online: 14 May 2024

References

- Asad, M., Dhanasekar, M., Zahra, T., & Thambiratnam, D. (2020). Impact mitigation of masonry walls with carbon fibre and auxetic fibre composite renders—A numerical study. *Structures*, 28, 2733–2751. <https://doi.org/10.1016/j.istruc.2020.09.047>
- Bohara, R. P., Linforth, S., Nguyen, T., Ghazlan, A., & Ngo, T. (2023). Anti-blast and -impact performances of auxetic structures: A review of structures, materials, methods, and fabrications. *Engineering Structures*, 276, 115377.
- Boonkong, T., Shen, Y. O., Guan, Z. W., & Cantwell, W. J. (2016). The low velocity impact response of curvilinear-core sandwich structures. *International Journal of Impact Engineering*, 93, 28–38. <https://doi.org/10.1016/j.ijimpeng.2016.01.012>
- Chen, Y., & Wang, Z. W. (2022). In-plane elasticity of the re-entrant auxetic hexagonal honeycomb with hollow-circle joint. *Aerospace Science and Technology*, 123, 107432. <https://doi.org/10.1016/j.ast.2022.107432>
- Coulais, C., Sabbadini, A., Vink, F., & van Hecke, M. (2018). Multi-step self-guided pathways for shape-changing metamaterials. *Nature*, 561, 512–515. <https://doi.org/10.1038/s41586-018-0541-0>
- Evans, K. E., Nkansah, M. A., Hutchinson, I. J., & Rogers, S. C. (1991). Molecular network design. *Nature*, 353, 124. <https://doi.org/10.1038/353124a0>
- Foster, L., Peketi, P., Allen, T., Senior, T., Duncan, O., & Alderson, A. (2018). Application of auxetic foam in sports helmets. *Applied Sciences*, 8, 354. <https://doi.org/10.3390/app8030354>
- Gao, Q., Li, W. B., Shi, Y., Liao, W.-H., Yin, G. D., Li, J. W., Wang, C. Y., & Qiu, R. X. (2023). A rotating auxetic energy harvester for vehicle wheels. *Engineering Structures*, 288, 116190. <https://doi.org/10.1016/j.engstruct.2023.116190>
- Gao, Q., Liao, W.-H., & Wang, L. (2020). An analytical model of cylindrical double-arrowed honeycomb with negative Poisson's ratio. *International Journal of Mechanical Sciences*, 173, 105400. <https://doi.org/10.1016/j.ijmecsci.2019.105400>
- Geramizadeh, H., Dariushi, S., & Salami, S. J. (2022). Optimal face sheet thickness of 3D printed polymeric hexagonal and re-entrant honeycomb sandwich beams subjected to three-point bending. *Composite Structures*, 291, 115618. <https://doi.org/10.1016/j.compstruct.2022.115618>
- Hamidin, F., Farrokhbadi, A., & Ahmadi, H. (2021). The effect of core shape on the bending response of sandwich panels with filled and unfilled sine and square corrugated cores. *Journal of Failure Analysis and Prevention*, 21, 537–546. <https://doi.org/10.1007/s11668-020-01098-z>
- He, Q., Li, L. Z., Jing, X. W., Jiang, Y. G., & Yan, D. J. (2023). Impact resistance analysis and multi-objective optimization of polyurea-coated auxetic honeycomb sandwich panels. *Materials Today Communications*, 35, 105577. <https://doi.org/10.1016/j.mtcomm.2023.105577>
- He, W. T., Lu, S. J., Yi, K., Wang, S. Q., Sun, G. Y., & Hu, Z. Q. (2019). Residual flexural properties of CFRP sandwich structures with aluminum honeycomb cores after low-velocity impact. *International Journal of Mechanical Sciences*, 161–162, 105026. <https://doi.org/10.1016/j.ijmecsci.2019.105026>
- Hou, Y., Tai, Y. H., Lira, C., Scarpa, F., Yates, J. R., & Gu, B. (2013). The bending and failure of sandwich structures with auxetic gradient cellular cores. *Composites Part A: Applied Science and Manufacturing*, 49, 119–131. <https://doi.org/10.1016/j.compositesa.2013.02.007>
- Li, W. T., Atsushi, D., Oh, Y. H., Jiratharanat, S., Wu, Z. A., & Chua, B. W. (2022). Influences of skin thickness, core topology, depth and direction on flexural deformation and ductile failure of Al honeycomb-based sandwich structures. *Composites Part B-Engineering*, 239, 109957. <https://doi.org/10.1016/j.compositesb.2022.109957>
- Li, Z. J., Wen, Y. F., Wen, X. L., Hao, H., & Chen, W. S. (2023). Single and double-layered kirigami corrugated sandwich panels against impact loads. *Structures*, 51, 402–414. <https://doi.org/10.1016/j.istruc.2023.03.074>
- Luo, H. C., Ren, X., Zhang, Y., Zhang, X. Y., Zhang, X. G., Luo, C., Cheng, X., & Xie, Y. M. (2022). Mechanical properties of foam-filled hexagonal and re-entrant honeycombs under uniaxial compression. *Composite Structures*, 280, 114922. <https://doi.org/10.1016/j.compstruct.2021.114922>
- Lv, W. T., Li, D., & Dong, L. (2020). Study on mechanical properties of a hierarchical octet-truss structure. *Composite Structures*, 249, 112640. <https://doi.org/10.1016/j.compstruct.2020.112640>
- Ma, M. Z., Yao, W. X., Jiang, W., Jin, W., Chen, Y., & Li, P. (2021). A multi-area fatigue damage model of composite honeycomb sandwich panels under three-point bending load. *Composite Structures*, 261, 113603. <https://doi.org/10.1016/j.compstruct.2021.113603>
- Naresh, K., Cantwell, W. J., Khan, K. A., & Umer, R. (2021). Single and multi-layer core designs for pseudo-ductile failure in honeycomb sandwich structures. *Composite Structures*, 256, 113059. <https://doi.org/10.1016/j.compsstruct.2020.113059>
- Ni, X.H., Jiang, W., Zhang, X.G., Han, D., Teng, X.C., Hao, J., Xu, H.H., & Ren, X. (2023). Quasi-static and dynamic properties studies of a metamaterial with enhanced auxeticity and tunable stiffness. *Composite Structures*, 321, 117254. <https://doi.org/10.1016/j.compstruct.2023.117254>
- Pan, J. W., Zhang, Q., Li, M., & Cai, J. G. (2024). A novel misplaced reinforced honeycomb with in-plane bidirectional enhancement. *International Journal of Mechanical Sciences*, 270, 109088. <https://doi.org/10.1016/j.ijmecsci.2024.109088>
- Peliński, K., & Smardzewski, J. (2022). Static response of synclastic sandwich panel with auxetic wood-based honeycomb cores subject to compression. *Thin-Walled Structures*, 179, 109559. <https://doi.org/10.1016/j.tws.2022.109559>
- Ren, X., Shen, J. H., Tran, P., Ngo, T. D., & Xie, Y. M. (2018). Design and characterization of a tuneable 3D buckling-induced auxetic metamaterial. *Materials and Design*, 139, 336–342. <https://doi.org/10.1016/j.matdes.2017.11.025>
- Rubino, V., Deshpande, V. S., & Fleck, N. A. (2010). The three-point bending of Y-frame and corrugated core sandwich beams. *International Journal of Mechanical Sciences*, 52, 485–494. <https://doi.org/10.1016/j.ijmecsci.2009.11.009>
- Sun, Z., Chen, H. J., Song, Z. W., Liu, H. Y., Cui, R. H., Guo, X., & Shi, S. S. (2021). Three-point bending properties of carbon fiber/honeycomb sandwich panels with short-fiber tissue and carbon-fiber belt interfacial toughening at different loading rate. *Composites Part A: Applied Science and Manufacturing*, 143, 106289. <https://doi.org/10.1016/j.compositesa.2021.106289>
- Vidwans, A., Trovalusci, P., Fantuzzi, N., & José, A. F. O. C. (2023). Application of column buckling theory to steel aluminium foam sandwich panels. *Structures*, 54, 607–617. <https://doi.org/10.1016/j.istruc.2023.04.112>
- Wang, L., Sun, J., Ding, T., Liang, Y., Ho, J. C. M., & Lai, M. H. (2022). Manufacture and behaviour of innovative 3D printed auxetic composite panels subjected to low-velocity impact load. *Structures*, 38, 910–933. <https://doi.org/10.1016/j.istruc.2022.02.033>

- Wang, Z. G., Li, Z. D., & Xiong, W. (2019a). Experimental investigation on bending behavior of honeycomb sandwich panel with ceramic tile face-sheet. *Composites Part B-Engineering*, 164, 280–286. <https://doi.org/10.1016/j.compositesb.2018.10.077>
- Wang, Z. G., Li, Z. D., & Xiong, W. (2019b). Numerical study on three-point bending behavior of honeycomb sandwich with ceramic tile. *Composites Part B-Engineering*, 167, 63–70. <https://doi.org/10.1016/j.compositesb.2018.11.108>
- Xia, F. K., Durandet, Y., Tan, P. J., & Ruan, D. (2022b). Three-point bending performance of sandwich panels with various types of cores. *Thin-Walled Structures*, 179, 109723. <https://doi.org/10.1016/j.tws.2022.109723>
- Xia, F. K., Pang, T., Sun, G. Y., & Ruan, D. (2022a). Longitudinal bending of corrugated sandwich panels with cores of various shapes. *Thin-Walled Structures*, 173, 109001. <https://doi.org/10.1016/j.tws.2022.109001>
- Xu, H. H., Luo, H. C., Zhang, X. G., Jiang, W., Teng, X. C., Chen, W. Q., Yang, J., Xie, Y. M., & Ren, X. (2023). Mechanical properties of aluminum foam filled re-entrant honeycomb with uniform and gradient designs. *International Journal of Mechanical Sciences*, 244, 108075. <https://doi.org/10.1016/j.ijmecsci.2022.108075>
- Yan, Z. C., Liu, Y., Yan, J. B., Wang, B. C., Bai, F., Shi, Z. Q., & Huang, F. L. (2022). Anti-blast performance of 3D-printed sandwich panels with auxetic hexagonal and regular hexagonal honeycomb cores. *Engineering Structures*, 272, 114996. <https://doi.org/10.1016/j.engstruct.2022.114996>
- Zhang, C. B., Lu, F. C., Wu, J., Zhang, K., Lin, B. C., & Qin, F. P. (2023). Research on three-point bending performance of hollow-core rod pyramidal gradient lattice sandwich beam. *Structures*, 57, 105165. <https://doi.org/10.1016/j.istruc.2023.105165>
- Zhao, X., Wei, L. L., Wen, D. W., Zhu, G. H., Yu, Q., & Ma, Z. D. (2021). Bending response and energy absorption of sandwich beams with novel auxetic honeycomb core. *Engineering Structures*, 247, 113204. <https://doi.org/10.1016/j.engstruct.2021.113204>

Publisher's Note

Springer Nature remains neutral with regard to jurisdictional claims in published maps and institutional affiliations.